A mycobacterial ABC transporter mediates the uptake of hydrophilic compounds

Rempel, Stephan; Gati, Cornelius; Nijland, Mark; Thangaratnarajah, Chancie; Karyolaimos, Alexandros; Gier, Jan-Willem L. de; Guskov, Albert; Slotboom, Dirk

Published in:
Nature

DOI:
10.1038/s41586-020-2072-8

Publication date:
2020

A mycobacterial ABC transporter mediates the uptake of hydrophilic compounds

https://doi.org/10.1038/s41586-020-2072-8

Received: 25 May 2019

Accepted: 8 January 2020

Published online: 25 March 2020

Check for updates

S. Rempel[1,7], C. Gati[2,3]✉, M. Nijland[1], C. Thangaratnarajah[1], A. Karyolaimos[4], J. W. de Gier[4], A. Guskov[1,5]✉ & D. J. Slotboom[1,6]✉

Mycobacterium tuberculosis (Mtb) is an obligate human pathogen and the causative agent of tuberculosis[1–3]. Although Mtb can synthesize vitamin B_{12} (cobalamin) de novo, uptake of cobalamin has been linked to pathogenesis of tuberculosis[2]. Mtb does not encode any characterized cobalamin transporter[4–6]; however, the gene *rv1819c* was found to be essential for uptake of cobalamin[1]. This result is difficult to reconcile with the original annotation of Rv1819c as a protein implicated in the transport of antimicrobial peptides such as bleomycin[7]. In addition, uptake of cobalamin seems inconsistent with the amino acid sequence, which suggests that Rv1819c has a bacterial ATP-binding cassette (ABC)-exporter fold[1]. Here, we present structures of Rv1819c, which reveal that the protein indeed contains the ABC-exporter fold, as well as a large water-filled cavity of about 7,700 Å^3, which enables the protein to transport the unrelated hydrophilic compounds bleomycin and cobalamin. On the basis of these structures, we propose that Rv1819c is a multi-solute transporter for hydrophilic molecules, analogous to the multidrug exporters of the ABC transporter family, which pump out structurally diverse hydrophobic compounds from cells[8–11].

To verify the cobalamin uptake activity of Rv1819c[1], we expressed the gene encoding Rv1819c in *Escherichia coli* ΔFEC, a strain that requires the presence of an uptake system for cobalamin to grow in the absence of methionine[5,6]; this system has been used to demonstrate cobalamin uptake activity of BtuCDF[4], BtuM[5] and ECF-CbrT[6]. Expression of Rv1819c in *E. coli* ΔFEC enabled the cells to grow in methionine-deficient medium supplemented with cobalamin (Fig. 1b, Extended Data Fig. 1e). To test whether transport is dependent on ATP hydrolysis, we mutated Glu576 of the Walker B motif to Gly. The mutant Rv1819c(E576G) was produced in *E. coli* at the same level as the wild-type protein (Fig. 1a), but did not allow growth of *E. coli* ΔFEC (Fig. 1b, Extended Data Fig. 1e).

The ATPase activity of some ABC transporters is stimulated in the presence of transported substrate[8,12,13], whereas others have uncoupled basal ATPase activity[4,12,14]. Using a coupled enzyme assay, we measured ATPase activity of Rv1819c that was reconstituted in liposomes. The protein exhibits basal ATPase activity of 0.53 ± 0.12 μmol ATP s^{-1} per μmol protein (mean ± s.e.m.) at an Mg–ATP concentration of 10 mM, whereas Rv1819c(E576G) exhibited background ATPase activity of 0.11 ± 0.03 μmol ATP s^{-1} per μmol protein (n = 5). In dodecyl-β-D-maltopyranoside (DDM) solution, Rv1819c showed approximately fivefold higher ATPase activity of 2.94 ± 0.19 μmol ATP s^{-1} per μmol protein (n = 3). To test whether the ATPase activity of Rv1819c in DDM was stimulated by the presence of substrate, we used a qualitative malachite green assay that is compatible with the presence of cobalamin, unlike the coupled enzyme assay (Fig. 1d). This assay revealed that the presence of cobalamin did not affect the ATPase activity. The Walker B mutant Rv1819c(E576G) exhibited background-level ATPase activity under all tested conditions (Fig. 1d).

To facilitate structural analysis, we aimed to trap the transporter in a defined conformation by using Rv1819c(E576G) in the presence of the non-hydrolysable ATP analogue adenylyl-5′-(β,γ-imido)triphosphate (AMP-PNP). A similar approach with other ABC transporters yielded structures in a conformation with tightly associated nucleotide-binding domains (NBDs)[13,15,16]. We obtained a 3D reconstruction at 3.5 Å resolution of a nucleotide-bound state (Fig. 2, Extended Data Fig. 2, Extended Data Table 1) using single-particle cryo-electron microscopy (cryo-EM) analysis. Extended Data Figure 3 shows an overview of the data-processing pipeline. Rv1819c(E576G) is homodimeric, with each protomer consisting of a transmembrane domain fused to an NBD. Although Rv1819c(E576G) exhibits the bacterial ABC-exporter fold, there are some prominent differences, including an additional N-terminal transmembrane helix 0 (TMH0; Fig. 2a), a 17-amino acid insertion breaking TMH3 (Extended Data Fig. 4a), an extracellular cap (Fig. 2a) and a large, occluded hydrophilic cavity (Fig. 2b, c). In our reconstruction, we observed a density for the detergent micelle around the protein, which enabled us to estimate the position of the membrane (Fig. 2a, Extended Data Fig. 4b). We also found density patches on the surface of Rv1819c(E576G), which resemble detergent or lipid molecules (Extended Data Fig. 5). The membrane-spanning part of Rv1819c is located between the 'elbow helix'—which connects TMH0 and TMH1—and is oriented parallel to the membrane plane on the intracellular side, and a loop rich in aromatic residues oriented parallel to the membrane on the extracellular side (Fig. 2a). The role of TMH0 is not apparent from the structure, but its position suggests

[1]Groningen Biomolecular Sciences and Biotechnology Institute (GBB), University of Groningen, Groningen, The Netherlands. [2]SLAC National Accelerator Laboratory, Menlo Park, CA, USA. [3]Department of Structural Biology, School of Medicine, Stanford University, Palo Alto, CA, USA. [4]Department of Biochemistry and Biophysics, Stockholm University, Stockholm, Sweden. [5]Moscow Institute of Physics and Technology, Dolgoprudny, Russia. [6]Zernike Institute for Advanced Materials, University of Groningen, Groningen, The Netherlands. [7]Present address: Structural Biology and Biophysics, Biozentrum–University of Basel, Basel, Switzerland. ✉e-mail: cgati@stanford.edu; a.guskov@rug.nl; d.j.slotboom@rug.nl

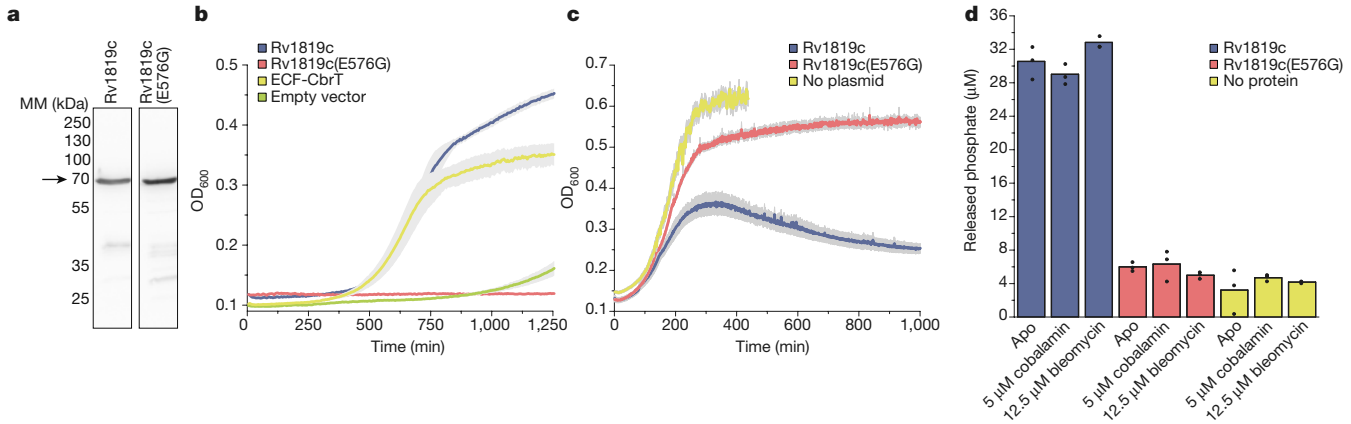

Fig. 1 | Import of cobalamin and bleomycin by Rv1819c and ATPase assay. **a**, Western blot of Rv1819c and Rv1819c(E576G) (arrow), showing that both proteins are expressed to a similar extent in *E. coli*. MM, molecular mass. The full image of the western blot is shown in Supplementary Fig. 1. **b**, Expression of Rv1819c (blue) or Rv1819c(E576G) (red) in *E. coli* ΔFEC shows that expression of the wild-type protein—but not the mutant—allows cells to grow in methionine-free conditions, indicating that Rv1819c-mediated import of cobalamin depends on ATP hydrolysis. As positive control, the cobalamine transporter ECF-CbrT was used[6] (yellow) and *E. coli* ΔFEC with an empty expression vector was used as negative control (green). Data are mean (lines) ± s.e.m. (grey area) of $n = 3$ biological replicates. **c**, *E. coli* JW0368 without plasmid is resistant to bleomycin (yellow). Expression of Rv1819c (blue) restores bleomycin sensitivity in *E. coli* JW0368, whereas cells expressing the mutant protein (red) remain resistant. Data are mean (lines) ± s.e.m. (grey area) of $n = 3$ biological replicates. **d**, Steady-state malachite green ATPase assay of Rv1819c (blue) in DDM solution shows that the protein exhibits basal ATPase activity, which is not stimulated by transported substrates. The ATP hydrolysis-inactive mutant (red) exhibits similar ATPase activity to the background (yellow) without added protein. Black dots show individual data points of $n = 3$ technical replicates.

that it may prevent lateral access to the cavity through the membrane. Lateral binding of hydrophobic substances is a feature of other ABC exporters, such as ABCB1[9].

Characteristically for the bacterial ABC-exporter fold, the NBDs are separated by a distance of around 22 Å from the intracellular membrane boundary by long α-helical extensions of TMH2–6 (Fig. 2a). On the extracellular side, TMH1, TMH2 and the N-terminal part preceding TMH0 extend out of the micelle by approximately 25 Å, forming a cap (Fig. 2a); this feature is not observed in other structurally characterized ABC exporters. The cap probably forms the extracellular gate.

The two identical NBDs are tightly associated—in a closed dimer conformation—with a Mg–AMP-PNP molecule in each active site (Fig. 2a, Extended Data Fig. 4c, d). The NBDs contain all the sequence motifs typical for ABC-transporter ATPases, apart from a noncanonical signature motif[12]. Non-standard signature motifs have been observed in other ABC transporters—in some cases, they cause loss of ATPase activity[17]. Because Rv1819c exhibits ATPase activity (Fig. 1d), we conclude that the ATPase sites are not degenerate. We also solved a structure of Rv1819c(E576G) that was purified in the absence of nucleotides (Extended Data Fig. 2, Extended Data Table 1), which is almost identical to the one purified in the presence of Mg–AMP-PNP (root mean square deviation (r.m.s.d.) of 0.49 Å). Of note, there was well-defined electron density in these nucleotide-binding sites, indicating the presence of a nucleotide triphosphate molecule (Extended Data Fig. 4e, f). These data indicate that the E576G mutant must have captured cellular Mg–ATP during protein production, and that Mg–ATP was not released or hydrolysed during the purification procedure. The mutation therefore appears to block ATPase activity completely, in contrast to Walker B mutations in other ABC transporters including BtuCDF[4].

Because of the higher resolution, we continue our discussion based on the Rv1819c(E576G) structure obtained in the presence of Mg–AMP-PNP. The protein contains an occluded cavity with a volume of more than 7,700 Å^3 (Fig. 2c), the largest found in structurally characterized ABC transporters to date[4,13,15]. The cavity spans the entire thickness of the membrane and extends into the intracellular part of the protein (Fig. 2c, Extended Data Fig. 4a). It consists of two connected chambers. The larger chamber is located in the transmembrane domain, and the smaller chamber is formed by the part of the protein that connects the NBDs and transmembrane domains (Fig. 2c, Extended Data Fig. 4a). The lower chamber is separated from the cytosol by Arg287 residues in TMH4 from the two protomers, and the upper chamber is sealed from the outside by the cap that protrudes from the membrane (Fig. 2f, g). Between the two chambers, the cavity is constricted at the level of the membrane boundary on the cytoplasmic side by the 17-amino-acid insertion in TMH3 (Fig. 2f, Extended Data Fig. 4a). The inner surface of the Rv1819c cavity is lined with polar and negatively charged residues, making it favourable for interactions with hydrophilic molecules (Fig. 2b), and has similar surface properties to the smaller cavities of the peptide transporters McjD and PCAT[13,15]. Comparison of Rv1819c with the ABC exporters McjD[13] and Sav1866[16] (in the Mg–AMP-PNP-bound states) shows that differences in the positions of TMH1 and TMH2 at the level of the outer leaflet of the lipid bilayer lead to the formation of either a cavity of different size (such as in Rv1819c and McjD) or two separate lobes that provide access to the bilayer environment (such as in Sav1866; Fig. 2d).

For transport to occur, the cavity must become accessible to the two sides of the membrane in an alternating manner (Fig. 2e). Structural studies of other ABC transporters suggest that the cytoplasmic gate of Rv1819c probably opens upon ATP hydrolysis and phosphate release, which allows the NBDs to be dissociated[18]. Opening of the extracellular gate may occur by a similar mechanism as in McjD, in which single-molecule FRET experiments showed that the gate opens spontaneously with short dwell times in the ATP-bound state[19]. The structure of the open-outward state might resemble that of the human lysosomal ABC transporter ABCD4, which was captured with an open external gate[20].

The cavity has a volume equal to that of six to seven cobalamin molecules, but there is no density for bound cobalamin. The absence of density for cobalamin is consistent with a lack of co-elution of the substrate with Rv1819c during co-purification experiments (Extended Data Fig. 6). Thus, there does not appear to be a specific high-affinity binding site, consistent with a predicted binding energy of −0.59 kcal mol^{-1} (Extended Data Fig. 7a). The lack of high-affinity substrate-binding sites makes it unlikely that multiple cobalamin molecules occupy the cavity at physiological concentrations.

Although we do not observe density for cobalamin in the cavity, it contains two well-defined symmetry-related patches of density, which may be peptides (Extended Data Fig. 7c, d); however, at this resolution it is not possible to unequivocally identify the molecules. We used mass

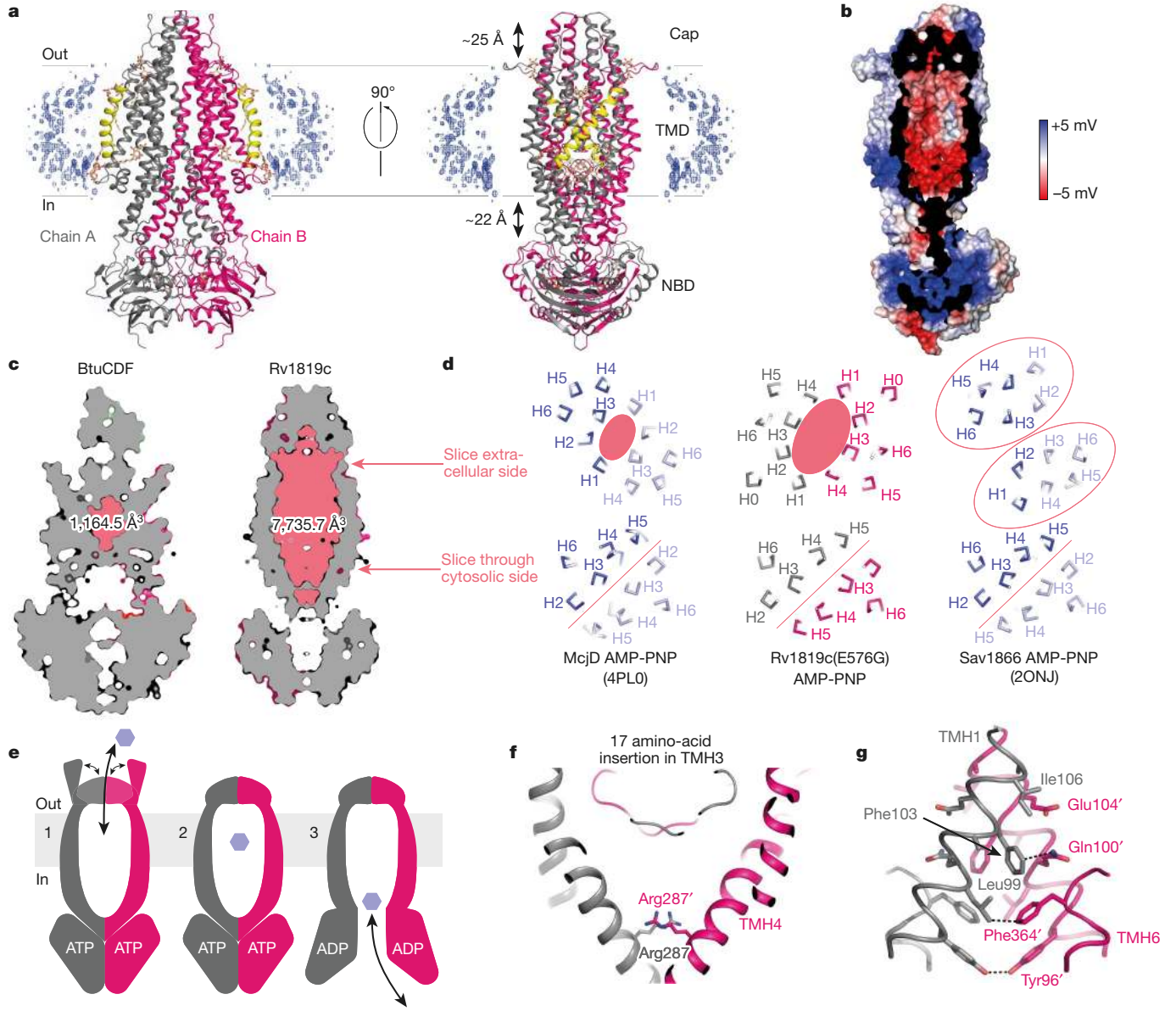

Fig. 2 | Structure of Mg–AMP-PNP-bound Rv1819c(E576G). a, Model of homodimeric Rv1819c(E576G). Grey, chain A; pink, chain B; yellow, TMH0 of both subunits. The membrane boundary is defined by the micelle belt (blue mesh). AMP-PNP and DDM molecules are shown in stick representation (wheat). TMD, transmembrane domain. **b**, Surface representation of Rv1819c(E576G), coloured according to electrostatic potential, in which the front protomer is removed to reveal the cavity surface. **c**, Slice-through representation of the internal cavities of BtuCDF (Protein Data Bank (PDB): 4FI3, left) and Rv1819c(E576G) (right, level of slices in **d** indicated by arrows). **d**, Comparison of the AMP-PNP-bound exporters McjD (PDB: 4PL0) and Sav1866 (PDB: 2ONJ; dark blue, chain A; light blue, chain B) with Rv1819c(E576G) (grey, chain A; pink, chain B). The slices at the cytosolic side show that the TMHs are arranged similarly, whereas differences are observed towards the extracellular side. McjD has a smaller cavity (indicated by red oval) than Rv1819c. In Sav1866, the helices form two lobes (red circles), allowing exported substrates to access the lipid bilayer. **e**, Hypothetical transport mechanism of Rv1819c. The transporter is depicted in cross-section (the monomers are coloured grey and pink, the membrane is shown in light grey). In the ATP-bound state (1) the NBDs form the closed dimer conformation and the extracellular gates open, possibly with short dwell times, to allow substrates (light blue) to enter. The intracellular side remains closed, preventing metabolites from entering. The substrate is captured (2)—this is the state we have solved structurally. Upon hydrolysis of ATP and release of inorganic phosphate (3), the NBD dimer dissociates and leads to opening of the intracellular gate, which allows the substrate to enter the cell. Subsequent binding of ATP resets the transporter. **f**, Proposed internal gate formed by Arg287 from each protomer (grey, chain A; pink, chain B). **g**, Proposed external gate (colouring as in **f**) formed by the cap.

spectrometry and de novo sequencing to identify potential peptides co-purifying with the protein (Supplementary Table 1). Several peptides were detected with high confidence, and we hypothesize that Rv1819c(E576G) co-purifies with peptides from the expression host or the culture medium.

Consistent with the presence of a peptide in the cavity, Rv1819c has been shown to be involved in the uptake of several antimicrobial peptides, including bleomycin[7]. *E. coli* takes up bleomycin via SbmA, and a disrupted *sbmA* locus leads to increased resistance to bleomycin[7]. Expression of Rv1819c restores sensitivity to bleomycin in *E. coli* JW0368 (*ΔsbmA::Km*^{R}), whereas cells expressing Rv1819c(E576G) are less susceptible (Fig. 1c). We conclude that bleomycin uptake by Rv1819c is dependent on ATP hydrolysis, even though it does not stimulate ATP hydrolysis (Fig. 1d). Docking into the cavity revealed that there is also no high-affinity binding site for bleomycin, similar to what was found for cobalamin (Extended Data Fig. 7b).

Our results suggest that Rv1819c is an uptake system for unrelated hydrophilic compounds, but there is likely to be some bias in the type of substrates that it transports. In particular, the negatively charged surface of the cavity might exclude anionic solutes. To test whether Rv1819c could mediate uptake of biotin, we expressed the gene encoding Rv1819c in *E. coli ΔbioH ΔyigM ΔsbmA::Km*^{R} (*E. coli* ΔHMA), a strain that requires the presence of an uptake system for biotin to grow and has been used to identify the biotin transporter BioY[21]. Biotin, like cobalamin, is needed only in small quantities for *E. coli* to grow[21,22]. Expression of Rv1819c did not restore growth of *E. coli* ΔHMA, showing that Rv1819c is not completely unselective (Extended Data Fig. 1a–d). The carboxylate group of biotin may make its entry into the cavity unfavourable. Similarly, the properties of the cavity may prevent the leakage of important compounds such as nucleotides from the cytoplasm. It is worth noting that specificity may also be imposed by the native environment of the protein in Mtb—for example, by the cell-wall structure[3].

In BtuCDF, the translocation pathway for cobalamin from the outside is sealed by a high-affinity substrate-binding protein (SBP), directing passage of the substrate through a low-affinity translocation chamber and into the cell[4,23]. SBPs are associated only with ABC importers[12,14], and it is not clear whether Rv1819c imposes directionality on transport. The results of the ATPase assays show that Rv1819c constantly hydrolyses ATP, which may lead to alternating opening of its cavity to the outside and inside of the cell, allowing the influx of substrates. Because of the lack of a high-affinity binding site, ATP hydrolysis might not lead to substrate accumulation by conversion of high-affinity to low-affinity states, but rather by causing conformational switching, thereby facilitating diffusion (Fig. 2e). Development of in vitro transport assays will be needed to address more detailed mechanistic questions.

Whereas dedicated high-specificity uptake systems, such as BtuCDF or McjD have translocation cavities that are sized to fit their substrates (cobalamin and the lasso-peptide MccJ25, respectively)[4,13] (Fig. 2c), a cavity that is much larger than the volume of any of the transported substrates may be characteristic for a non-specific transporter. Physiologically, nonspecific importers are likely to transport substrates with low efficiency, but Rv1819c may be sufficient as a sole transporter for cobalamin because Mtb is an extremely slow-growing organism. The existence of such nonspecific importers may also explain how antibiotics cross the inner membrane and, in some cases, accumulate in bacterial cells[24]. This is generally thought to occur by passive diffusion, but it is difficult to reconcile with uptake of large and hydrophilic antibiotic classes such as aminoglycosides[24]. Because Rv1819c is—to some extent—functionally interchangeable with SbmA and BacA[7,25], nonspecific importers could be more widespread among prokaryotes. This could make unspecific importers potential targets to, for example, enhance the uptake of antimicrobial compounds.

Online content

Any methods, additional references, Nature Research reporting summaries, source data, extended data, supplementary information, acknowledgements, peer review information; details of author contributions and competing interests; and statements of data and code availability are available at https://doi.org/10.1038/s41586-020-2072-8.

1. Gopinath, K. et al. A vitamin B_{12} transporter in *Mycobacterium tuberculosis*. *Open Biol.* **3**, 120175 (2013).
2. Gopinath, K., Moosa, A., Mizrahi, V. & Warner, D. F. Vitamin B_{12} metabolism in *Mycobacterium tuberculosis*. *Future Microbiol.* **8**, 1405–1418 (2013).
3. Jankute, M., Cox, J. A. G., Harrison, J. & Besra, G. S. Assembly of the mycobacterial cell wall. *Annu. Rev. Microbiol.* **69**, 405–423 (2015).
4. Korkhov, V. M., Mireku, S. A. & Locher, K. P. Structure of AMP-PNP-bound vitamin B_{12} transporter BtuCD-F. *Nature* **490**, 367–372 (2012).
5. Rempel, S., Colucci, E., de Gier, J. W., Guskov, A. & Slotboom, D. J. Cysteine-mediated decyanation of vitamin B_{12} by the predicted membrane transporter BtuM. *Nat. Commun.* **9**, 3038 (2018).
6. Santos, J. A. et al. Functional and structural characterization of an ECF-type ABC transporter for vitamin B_{12}. *eLife* **7**, e35828 (2018).
7. Domenech, P., Kobayashi, H., LeVier, K., Walker, G. C. & Barry, C. E. III. BacA, an ABC transporter involved in maintenance of chronic murine infections with *Mycobacterium tuberculosis*. *J. Bacteriol.* **191**, 477–485 (2009).
8. Shukla, S., Abel, B., Chufan, E. E. & Ambudkar, S. V. Effects of a detergent micelle environment on P-glycoprotein (ABCB1)–ligand interactions. *J. Biol. Chem.* **292**, 7066–7076 (2017).
9. Aller, S. G. et al. Structure of P-glycoprotein reveals a molecular basis for poly-specific drug binding. *Science* **323**, 1718–1722 (2009).
10. Kim, Y. & Chen, J. Molecular structure of human P-glycoprotein in the ATP-bound, outward-facing conformation. *Science* **359**, 915–919 (2018).
11. Alam, A., Kowal, J., Broude, E., Roninson, I. & Locher, K. P. Structural insight into substrate and inhibitor discrimination by human P-glycoprotein. *Science* **363**, 753–756 (2019).
12. ter Beek, J., Guskov, A. & Slotboom, D. J. Structural diversity of ABC transporters. *J. Gen. Physiol.* **143**, 419–435 (2014).
13. Choudhury, H. G. et al. Structure of an antibacterial peptide ATP-binding cassette transporter in a novel outward occluded state. *Proc. Natl Acad. Sci. USA* **111**, 9145–9150 (2014).
14. Rempel, S., Stanek, W. K. & Slotboom, D. J. ECF-type ATP-binding cassette transporters. *Annu. Rev. Biochem.* **88**, 551–576 (2019).
15. Lin, D. Y., Huang, S. & Chen, J. Crystal structures of a polypeptide processing and secretion transporter. *Nature* **523**, 425–430 (2015).
16. Dawson, R. J. P. & Locher, K. P. Structure of the multidrug ABC transporter Sav1866 from *Staphylococcus aureus* in complex with AMP-PNP. *FEBS Lett.* **581**, 935–938 (2007).
17. Chen, M., Abele, R. & Tampé, R. Functional non-equivalence of ATP-binding cassette signature motifs in the transporter associated with antigen processing (TAP). *J. Biol. Chem.* **279**, 46073–46081 (2004).
18. Hofmann, S. et al. Conformation space of a heterodimeric ABC exporter under turnover conditions. *Nature* **571**, 580–583 (2019).
19. Husada, F. et al. Conformational dynamics of the ABC transporter McjD seen by single-molecule FRET. *EMBO J.* **37**, e100056 (2018).
20. Xu, D. et al. Cryo-EM structure of human lysosomal cobalamin exporter ABCD4. *Cell Res.* **29**, 1039–1041 (2019).
21. Finkenwirth, F., Kirsch, F. & Eitinger, T. Solitary BioY proteins mediate biotin transport into recombinant *Escherichia coli*. *J. Bacteriol.* **195**, 4105–4111 (2013).
22. Choi-Rhee, E. & Cronan, J. E. Biotin synthase is catalytic in vivo, but catalysis engenders destruction of the protein. *Chem. Biol.* **12**, 461–468 (2005).
23. Korkhov, V. M., Mireku, S. A., Veprintsev, D. B. & Locher, K. P. Structure of AMP-PNP-bound BtuCD and mechanism of ATP-powered vitamin B_{12} transport by BtuCD-F. *Nat. Struct. Mol. Biol.* **21**, 1097–1099 (2014).
24. Taber, H. W., Mueller, J. P., Miller, P. F. & Arrow, A. S. Bacterial uptake of aminoglycoside antibiotics. *Microbiol. Rev.* **51**, 439–457 (1987).
25. Runti, G. et al. Functional characterization of SbmA, a bacterial inner membrane transporter required for importing the antimicrobial peptide Bac7(1-35). *J. Bacteriol.* **195**, 5343–5351 (2013).

Methods

No statistical methods were used to predetermine sample size. The experiments were not randomized. The investigators were not blinded to allocation during experiments and outcome assessment.

Molecular methods

For expression, a codon-optimized version of Rv1819c from *M. tuberculosis* H37Rv with a C-terminal His_8-tag was cloned into pBAD24 with NcoI and HindIII restriction sites in-frame with the start codon of the NcoI restriction site. The E576G mutation was introduced using site-directed mutagenesis. All constructs were sequenced to confirm correctness. All primers used are listed in Extended Data Table 2.

Construction of *E. coli ΔbioH ΔyigM ΔsbmA::Km^R*

The triple-knockout strain was constructed as previously described[5,6] by P1-mediated phage transduction[26]. *E. coli* strains JW0368 (*ΔsbmA::Km^R*), JW3803 (*ΔyigM*) and JW3375 (*ΔbioH*) from the Keio collection[27] served as starting point. The triple-knockout strain was cultivated with 1 μM L-biotin supplementation in all media.

Growth assays

The cobalamin-dependent-growth assay was performed as described[5,6], using *E. coli* ΔFEC transformed with expression plasmids for Rv1819c and Rv1819c(E576G). The biotin-dependent-growth assay was conducted in the same way with the following adaptations. The strain was always cultured in the presence of 1 μM L-biotin before the growth assay. Before inoculating the growth assay, the pre-culture was washed three times with plain M9 medium to remove biotin carry over. In the growth assay, the strain was supplemented with biotin at the concentration specified in the text and no cobalamin was added. The bleomycin-sensitivity assay was carried out with *E. coli* JW0368 (*ΔsbmA::Km^R*) cells from the Keio[27] collection and the same expression constructs. Cells were grown in LB medium supplemented with 25 μg ml^{-1} kanamycin, 100 μg ml^{-1} ampicillin, 0.0002% L-arabinose and 5 μM bleomycin sulfate (70% bleomycin A_2 and 30% bleomycin B_2; Sigma Aldrich) shaking at 37 °C in a BioTek Powerwave340 plate reader. The strain without plasmid was grown in the absence of ampicillin and with 0.00002% L-arabinose. Then, 200 μl of medium was added to a sterile 96-well plate (Cellstar) and inoculated at a 1:100 ratio from an overnight pre-culture (same medium without L-arabinose and bleomycin). The plates were covered with a gas-permeable foil (Diversified Biotech) and the optical density at 600 nm was measured every minute.

Expression and crude membrane vesicle preparation

Expression of Rv1819c variants was done as described[5], with the following adaptations: for the main cultures, baffled flasks were used and expression was induced with 0.02% L-arabinose.

Western blot analysis

Crude membrane vesicles were analysed by SDS–PAGE followed by semi-dry western blotting. The used antibody was a mouse monoclonal polyhistidine peroxidase-conjugated antibody (Sigma-Aldrich, A7058) and was added in a 1:6,000 dilution. The blot was developed using SuperSignal West Pico PLUS Chemiluminescent Substrate (Thermo Fisher).

Purification of Rv1819c

The protein was solubilized in buffer A (50 mM MES–NaOH pH 7.0, 300 mM NaCl, 15 mM imidazole–HCl pH 7.0 and 1% DDM) for 45 min at 4 °C with gentle agitation. Unsolubilized material was removed by centrifugation for 25 min at 219,373*g* at 4 °C. The supernatant was decanted into a poly-prep column (BioRad) containing 0.5 ml bed volume of either fast-flow Ni^{2+} Sepharose (for biochemical studies, GE Healthcare) or Ni^{2+}-NTA His Bind Superflow Resin (for cryo-EM studies, EMD Millipore), which was equilibrated with 10 ml buffer A containing no DDM. Binding was allowed to occur for 1 h at 4 °C with gentle agitation and unbound material was allowed to flow through. The column was washed with 10 ml buffer A supplemented with 60 mM imidazole–HCl pH 7.0 and 0.5% DDM. The protein was eluted in buffer A supplemented with 350 mM imidazole–HCl pH 7.0 and 0.015% DDM. The elution fraction containing most protein was loaded on a Superdex 200 10/300GL Increase (GE Healthcare) size-exclusion column that was equilibrated with 30 ml buffer B (50 mM MES–NaOH pH 6.5, 200 mM NaCl and 0.015% DDM). Elution was done in the same buffer and the peak fractions were used for structural and biochemical studies. For the co-elution experiment, buffer A was additionally supplemented with 2 mM cyano-cobalamin (Acros Organics) and 5 mM Mg–ATP or 5 mM Mg–AMP-PNP (the latter only for elution from the immobilized metal affinity chromatography column).

Cryo-EM sample preparation, data collection and image processing

Rv1819c(E576G) was concentrated to 10.3 mg ml^{-1} with a 0.5 ml 100-kDa cut-off Amicon Ultra (Millipore) concentrator, by centrifugation (14,000*g* at 4 °C). Stock solutions of $MgCl_2$ and AMP-PNP (Roche) were added to achieve a final concentration of 5 mM. Then, 3 μl of the final sample was applied to a freshly glow-discharged (easiGlow, Ted Pella, 15 mA, 30 s) holey-carbon cryo-EM grid (Quantifoil Au R1.2/1.3, 300 mesh). The apo sample was treated the same way, but was only concentrated to 3.7 mg ml^{-1} and no nucleotides were added. Grids were blotted for 5 s in a Leica EM GP at 20 °C and 100% relative humidity and plunge-frozen into liquid ethane. Grids were stored in liquid nitrogen until use. Automatic data collection was performed on a Titan Krios microscope (Thermo Fisher), equipped with a K3 direct-electron detector (Gatan), using the serialEM software package[28]. A total of 8,620 videos were collected with a frame duration of 70 ms, a total exposure time of 3.01 s, a dose rate of ~20 e^- pixel^{-1} s^{-1}, and pixel size of 0.42605 Å in super-resolution mode. Image processing was performed using RELION 3.0[29]. Beam-induced motion correction was performed using the RELION internal wrapper for MotionCor2, applying bin = 2 (ref. [30]), and CtfFind4.1 was used for CTF estimation[31]. Particle picking was done using the reference-free picking algorithm, yielding a total of 3,500,000 picks. The latter were extracted with an additional binning factor of 2 and were applied to several rounds of 2D classification resulting in 870,407 particles. Re-extraction of particles (bin = 1) and two rounds of 3D classification yielded the final subset of 314,691 particles. Per particle, CTF estimates and Bayesian polishing yielded a final resolution of 3.5 Å. Map sharpening was performed with Phenix Autosharpen v.1.14[32] with an overall *B*-factor of 136 Å^2. The general processing pipeline is depicted in Extended Data Fig. 2.

The apo dataset was collected and processed with identical instruments, setup and software packages. A total of 1,036 micrographs was collected, resulting in an initial 354,241 particle picks after reference-free autopicking. Several rounds of 2D and 3D classification yielded a final dataset of 35,890 particles, which was reconstructed to 4.3 Å final resolution applying C2 symmetry.

Model building and docking

The model was built manually into the obtained map using COOT[33] v.0.8.9.2. Refinement was performed in Phenix v.1.14[32] with final model validation in MolProbity[34]. At the present resolution, the presence of magnesium ions in a nucleotide–magnesium complex cannot be directly deduced from the data; however, the complex was allowed to form by mixing equimolar amounts of $MgCl_2$ and AMP-PNP before use. Cellular nucleotides only exist in complex with magnesium. Electrostatic potentials were calculated using the Pymol v.2.3 ABPS plugin[35]. Structure images were prepared with Pymol v.2.3, cavities were calculated using the CASTp[36] server with a probe radius of 1.5 Å and volumes were calculated using UCSF Chimera. Docking with bleomycin and

cobalamin was done using AutoDockTools v1.5 in combination with Autodock v.4.2[37].

Reconstitution into liposomes and coupled enzyme ATPase assay

Purified Rv1819c and Rv1819c(E576G) were reconstituted as described previously[6,38], in a 1:500 (w/w) ratio. The proteoliposomes were prepared as described without loading the lumen and were added to the reaction solution resulting in a final volume of 200 µl in a 96-well plate (Cellstar) with 1.67 µg protein (proteoliposomes) or 5 µg protein (detergent solution) in every reaction. The coupled enzyme assay contained 10 mM $MgCl_2$, 10 mM ATP (Roche), 0.6 mM NADH (Sigma Aldrich), 4 mM phosphoenolpyruvate (Roth), 35 µl pyruvate kinase–lactic dehydrogenase solution (Sigma Aldrich) and 50 mM potassium phosphate pH 7.5. ATPase activity was followed by monitoring the decrease in NADH concentration. The concentration of NADH was calculated using Beer–Lambert law with $\varepsilon = 6220\ cm^{-1}\ M^{-1}$ at 340 nm and the length of the light path through the solution was determined by measuring the absorption (A) of 200 µl water at 977 nm and 900 nm. The length of the light path was $(A_{977\,nm} - A_{900\,nm}) \times 0.18^{-1}$ cm. Additionally, a random distribution of right-side in and right-side out reconstituted protein was assumed, resulting in a protein concentration of 0.83 µg. All experiments were performed as technical triplicates and given rates of the reconstituted proteins are corrected for basal activity of the reactions without proteoliposomes.

Malachite green assay

ATPase activity was allowed to proceed for 20 min at 37 °C with 0.1 mg ml^{-1} detergent-solubilized Rv1819c or Rv1819c(E576G) in buffer B, which was supplemented with 312.5 µM $MgCl_2$ and 312.5 µM ATP. The reaction volume was 160 µl in 96-well plates. Substrates were added to the indicated concentrations as specified in the main text. Then, 1.25 mM K–EDTA was added to quench the reaction before adding 40 µl Malachite Green Phosphate Assay Kit working solution (Sigma Aldrich). Colour was allowed to develop for 30 min at room temperature before measuring the level of ATPase activity at 640 nm. All experiments were performed as technical triplicates. Phosphate concentrations were calculated from a standard curve obtained with the supplied phosphate standard of the kit.

Mass spectrometry and de novo sequencing

Purified Rv1819c (50 µl) was concentrated using a C18-Stage tip (Thermo Fisher) and eluted in 10 µl 33% acetonitrile and 0.1% trifluoroacetic acid. The sample was tenfold diluted in 5% formic acid and subjected to an Ultimate 3000 nano-HPLC system (Thermo Fisher) coupled online to a Q-Exactive Plus mass spectrometer with a NanoFlex source (Thermo Fisher) equipped with a stainless-steel emitter. Then, 3 µl of sample was loaded with a flow rate of 0.02 ml min^{-1} in 0.1% formic acid on a 5 mm by 0.3 mm trapping column packed with PepMAP100 5-µm particles (Dionex). After 3 min, peptides were forward-eluted onto a 50 cm by 0.075 mm column packed with Acclaim C18 PepMAP100 2-µm particles (Dionex). The mobile phase gradient was delivered at a flow rate of 0.3 µl min^{-1} with increasing solvent B (acetonitrile, 0.1% formic acid) from 2% to 80% within 15 min, held at 80% for 5 min, returned to 2% within 1 min, and held at 3% solvent A (0.1% formic acid) for 19 min. Mass spectrometry data were acquired using data-dependent top-5 method, dynamically choosing the most-abundant not-yet-sequenced precursor ions from the survey scans (300–3,000 Th) with a dynamic exclusion of 3 s. Isolation of precursors was performed with a window of 2 Da. Survey scans were acquired at a resolution of 70,000 at m/z 200. Resolution for higher-energy collisional dissociation spectra was set to 17,500 at m/z 200 with a maximum ion-injection time of 50 ms. The S-lens RF level was set at 60 and the capillary temperature was set at 250 °C. Precursor ions with five or higher charges were excluded from fragmentation selection. De novo sequencing was performed using Peaks Studio 10 (Bioinformatics Solutions) set to a parent mass error tolerance of 20 ppm, a fragment mass error of 0.04 Da, methionine as variably oxidizable, and no enzyme treatment.

Reporting summary

Further information on research design is available in the Nature Research Reporting Summary linked to this paper.

Data availability

Atomic coordinates and the cryo-EM map are deposited in the Protein Data Bank under accession numbers 6TQF (AMP-PNP) and 6TQE (purified without addition) and in the Electron Microscopy Data Bank under accession numbers EMD-10550 (AMP-PNP), EMD-10549 (purified without addition), respectively. Source Data for Fig. 1 and Extended Data Figs. 1, 6 are available with this paper. The other data from this study are available from the corresponding authors upon reasonable request.

26. Thomason, L. C., Costantino, N. & Court, D. L. *E. coli* genome manipulation by P1 transduction. *Curr. Protoc. Mol. Biol.* **79**, 1.17.1–1.17.8 (2007).
27. Baba, T. et al. Construction of *Escherichia coli* K-12 in-frame, single-gene knockout mutants: the Keio collection. *Mol. Syst. Biol.* **2**, 2006.0008 (2006).
28. Schorb, M., Haberbosch, I., Hagen, W. J. H., Schwab, Y. & Mastronarde, D. N. Software tools for automated transmission electron microscopy. *Nat. Methods* **16**, 471–477 (2019).
29. Zivanov, J. et al. New tools for automated high-resolution cryo-EM structure determination in RELION-3. *eLife* **7**, e42166 (2018).
30. Zheng, S. Q. et al. MotionCor2: anisotropic correction of beam-induced motion for improved cryo-electron microscopy. *Nat. Methods* **14**, 331–332 (2017).
31. Rohou, A. & Grigorieff, N. CTFFIND4: fast and accurate defocus estimation from electron micrographs. *J. Struct. Biol.* **192**, 216–221 (2015).
32. Adams, P. D. et al. PHENIX: a comprehensive Python-based system for macromolecular structure solution. *Acta Crystallogr. D* **66**, 213–221 (2010).
33. Emsley, P., Lohkamp, B., Scott, W. G. & Cowtan, K. Features and development of Coot. *Acta Crystallogr. D* **66**, 486–501 (2010).
34. Chen, V. B. et al. MolProbity: all-atom structure validation for macromolecular crystallography. *Acta Crystallogr. D* **66**, 12–21 (2010).
35. Baker, N. A., Sept, D., Joseph, S., Holst, M. J. & McCammon, J. A. Electrostatics of nanosystems: application to microtubules and the ribosome. *Proc. Natl Acad. Sci. USA* **98**, 10037–10041 (2001).
36. Tian, W., Chen, C., Lei, X., Zhao, J. & Liang, J. CASTp 3.0: computed atlas of surface topography of proteins. *Nucleic Acids Res.* **46** (W1), W363–W367 (2018).
37. Morris, G. M. et al. AutoDock4 and AutoDockTools4: automated docking with selective receptor flexibility. *J. Comput. Chem.* **30**, 2785–2791 (2009).
38. Geertsma, E. R., Nik Mahmood, N. A. B., Schuurman-Wolters, G. K. & Poolman, B. Membrane reconstitution of ABC transporters and assays of translocator function. *Nat. Protoc.* **3**, 256–266 (2008).

Acknowledgements We thank M. Heinemann and S. Bonsing-Vedelaar for providing the strains from the Keio collection; L. Hielkema for help with purification optimization; A. Garaeva for support with screening-grid preparation and preparing lipid solutions; I. van 't Land-Kuper for support with growth assays and protein purifications; R. Singh for design of the codon-optimized construct; the SLAC-Stanford Cryo-EM center (SLAC National Accelerator Laboratory), where the dataset was recorded, for microscope time; E. A. Montabana for microscope support; and Y.-T. Li for support with computing resources. We acknowledge support from the cryo-EM and mass spectrometry facilities of the University of Groningen. This study was supported by the European Molecular Microbiology Organization (EMBO short-term fellowship ASTF-382-2015 to S.R.), the Netherlands Organisation for Scientific Research (NWO-TOP grant 714.018.003 to D.J.S. and NWO Vidi grant 723.014.002 to A.G.), the Swedish Research Council and the Carl Tryggers Foundation (2015-05288 and CTS17:114, respectively, to J.W.d.G), and the Department of Energy, Laboratory Directed Research and Development program at SLAC National Accelerator Laboratory, under contract DE-AC02-76SF00515.

Author contributions All authors designed experiments. S.R. conducted cloning and growth assays, S.R., C.T. and M.N. performed biochemical assays. S.R. and A.G. built the model. S.R., A.K. and J.W.d.G. constructed knockout strains. C.G. collected and processed cryo-EM data. All authors analysed data. S.R. and D.J.S. wrote the manuscript with input from all authors.

Competing interests The authors declare no competing interests.

Additional information

Supplementary information is available for this paper at https://doi.org/10.1038/s41586-020-2072-8.

Correspondence and requests for materials should be addressed to C.G., A.G. or D.J.S.

Peer review information *Nature* thanks Damian Ekiert, Eric Rubin and Jochen Zimmer for their contribution to the peer review of this work.

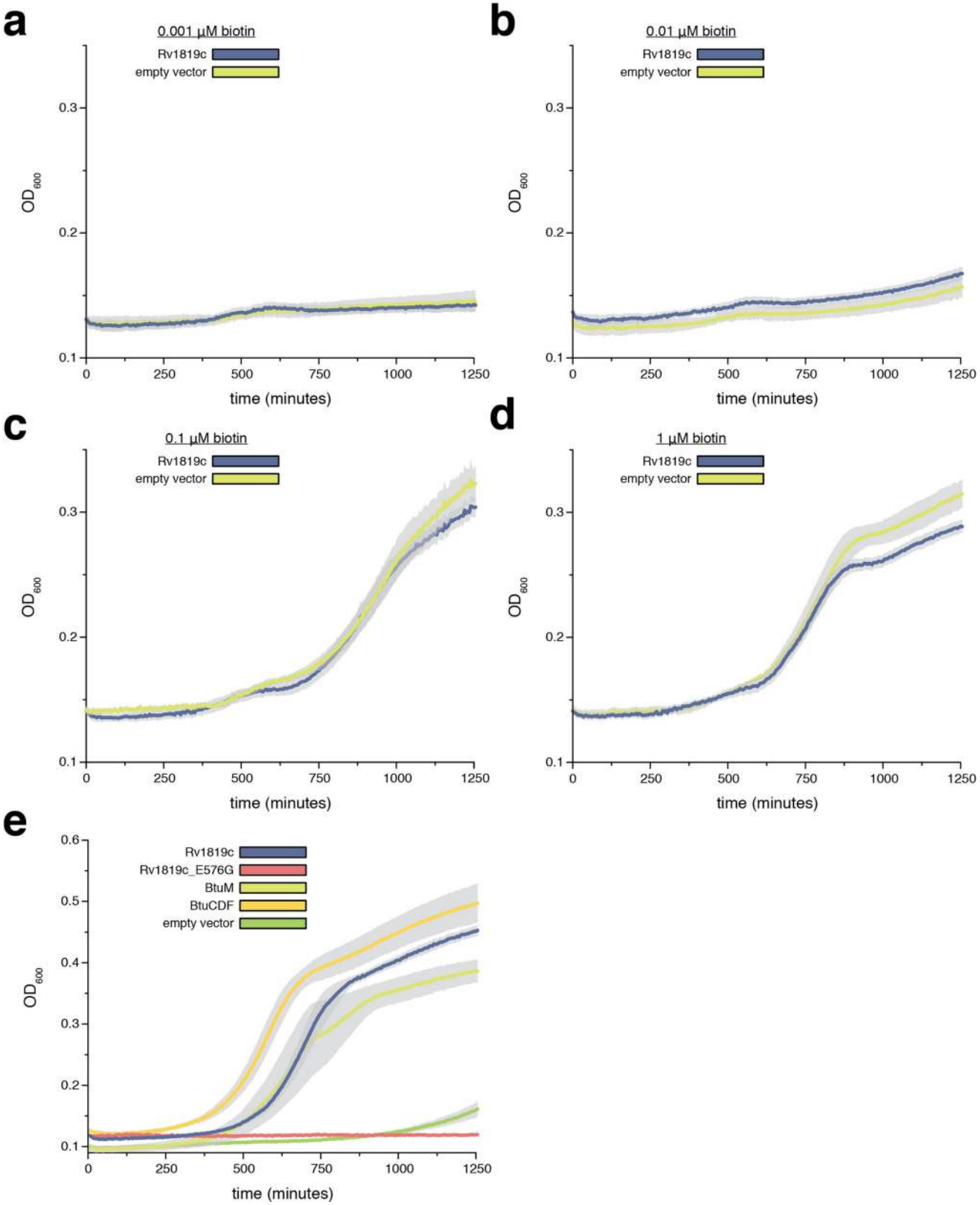

Extended Data Fig. 1 | Biotin-dependent-growth assay with *E. coli* Δ*bioH* Δ*yigM* Δ*sbmA*::*Km*^{R} and cobalamin-dependent-growth assay with additional controls. a–**d**, The mutant strain expressing either Rv1819c (blue) or carrying the empty expression vector pBAD24 (yellow) was grown in the presence of 0.001 µM biotin (**a**), 0.01 µM biotin (**b**), 0.1 µM biotin (**c**) or 1 µM biotin (**d**). There is no difference between Rv1819c-expressing cells and cells without Rv1819c, whereas cells expressing the *E. coli* biotin transporter YigM can grow under these conditions[21]. The grey area shows the s.e.m. of biological triplicates. **e**, Growth curves for Rv1819c (blue), Rv1819c(E576G) (red) and the empty vector (pBAD24, green) are shown as in Fig. 1b. Additional control curves from the cobalamin transporter BtuM (yellow) and ABC transporter BtuCDF (orange) are included for better comparison. The grey area shows the s.e.m. of the mean (lines) of $n = 3$ biological triplicates.

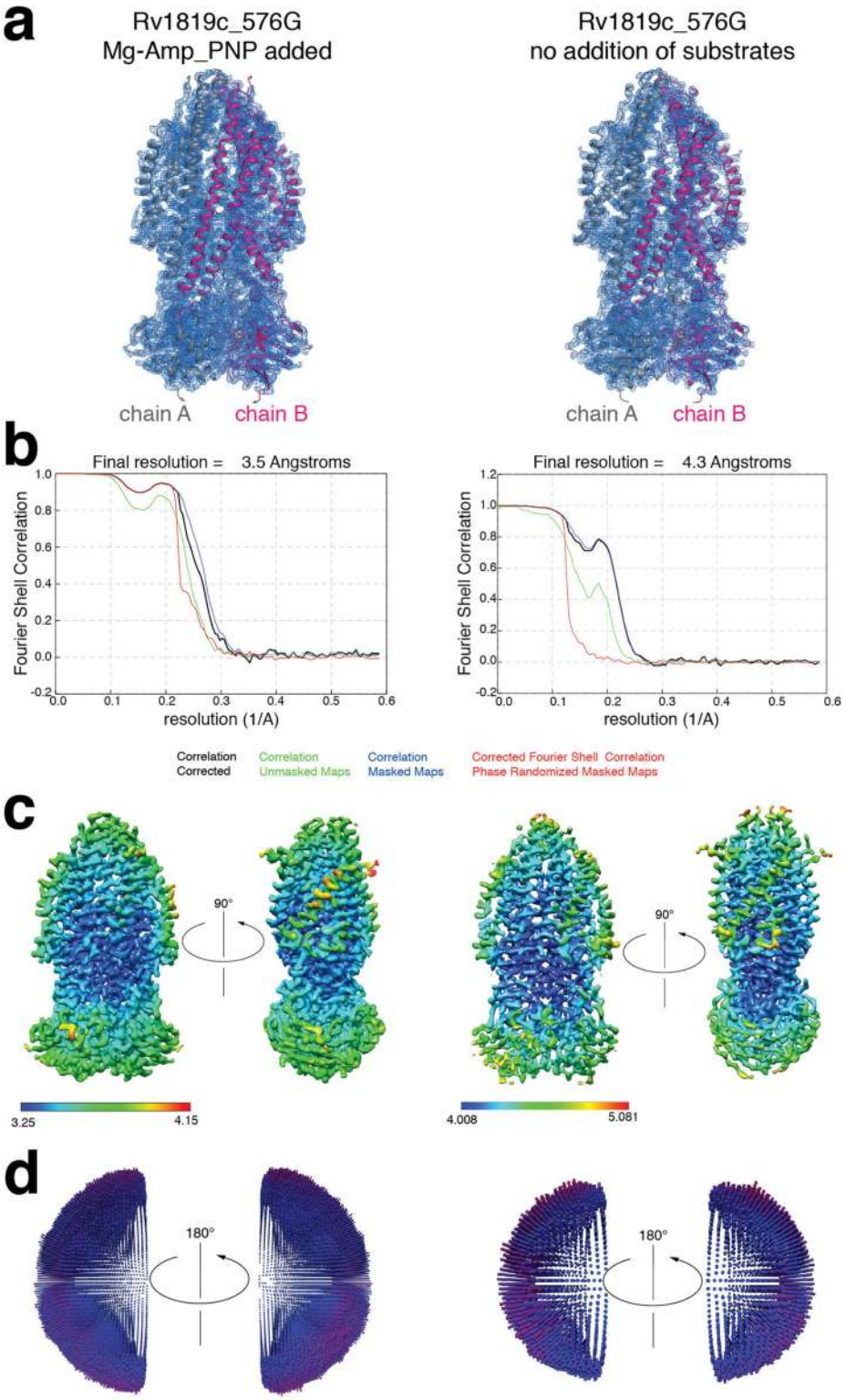

Extended Data Fig. 2 | Resolution and angular distribution of the cryo-EM 3D reconstructions. a, Comparison of the structures obtained in the presence (left) or absence (right) of added Mg–AMP-PNP and their corresponding densities (blue mesh). Representation of nucleotides as in Fig. 2a. **b**, Fourier shell correlation plot for Rv1819c(E576G) Mg–AMP-PNP (314,691 particles, left) and Rv1819c(E576G) without addition of substrates (35,890 particles, right). **c**, Maps (without micelle belt) of both structures in front view (left) and side view (right, rotated by 90°), coloured according to local resolution, from blue (3.25 Å and 4.008 Å) to red (4.15 Å and 5.081 Å). **d**, Angular distribution of views in the 3D reconstruction with applied C2 symmetry (left view and right view, rotated by 180°).

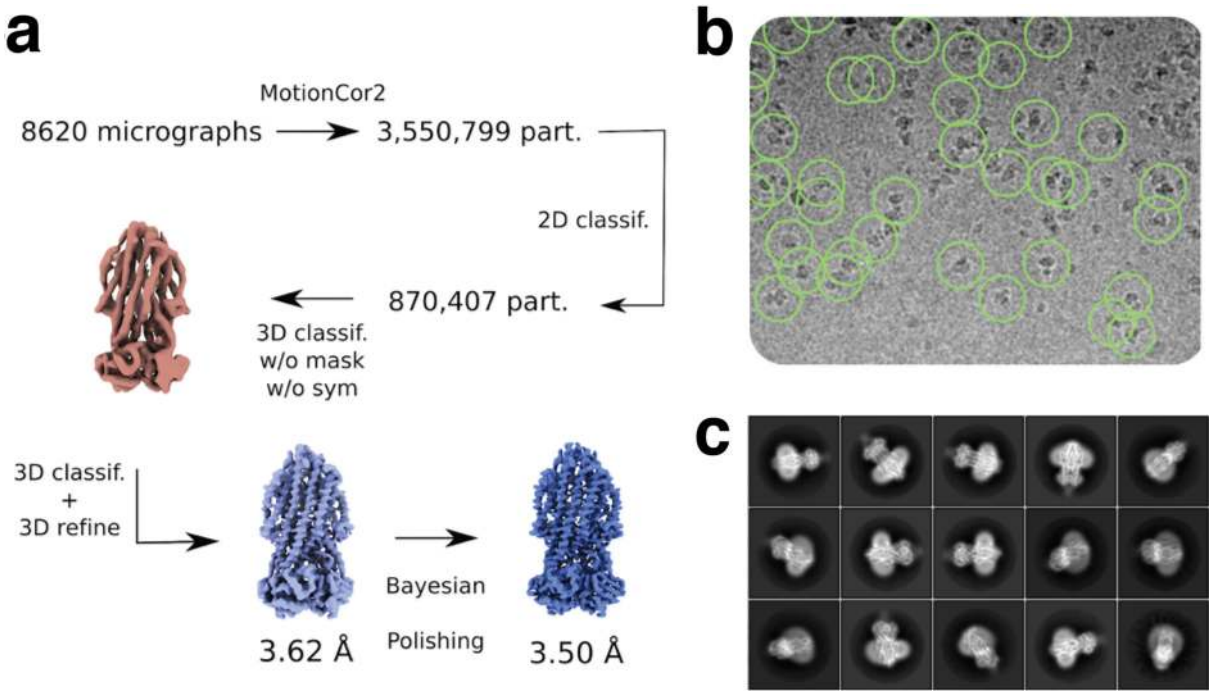

Extended Data Fig. 3 | Cryo-EM data-processing workflow for Rv1819c(E576G) with Mg–AMP-PNP. a, Single-particle cryo-EM data-processing scheme using RELION3.0. **b**, Representative micrograph showing picked particles (indicated by green circles). **c**, Two-dimensional class averages show distinct secondary structure features.

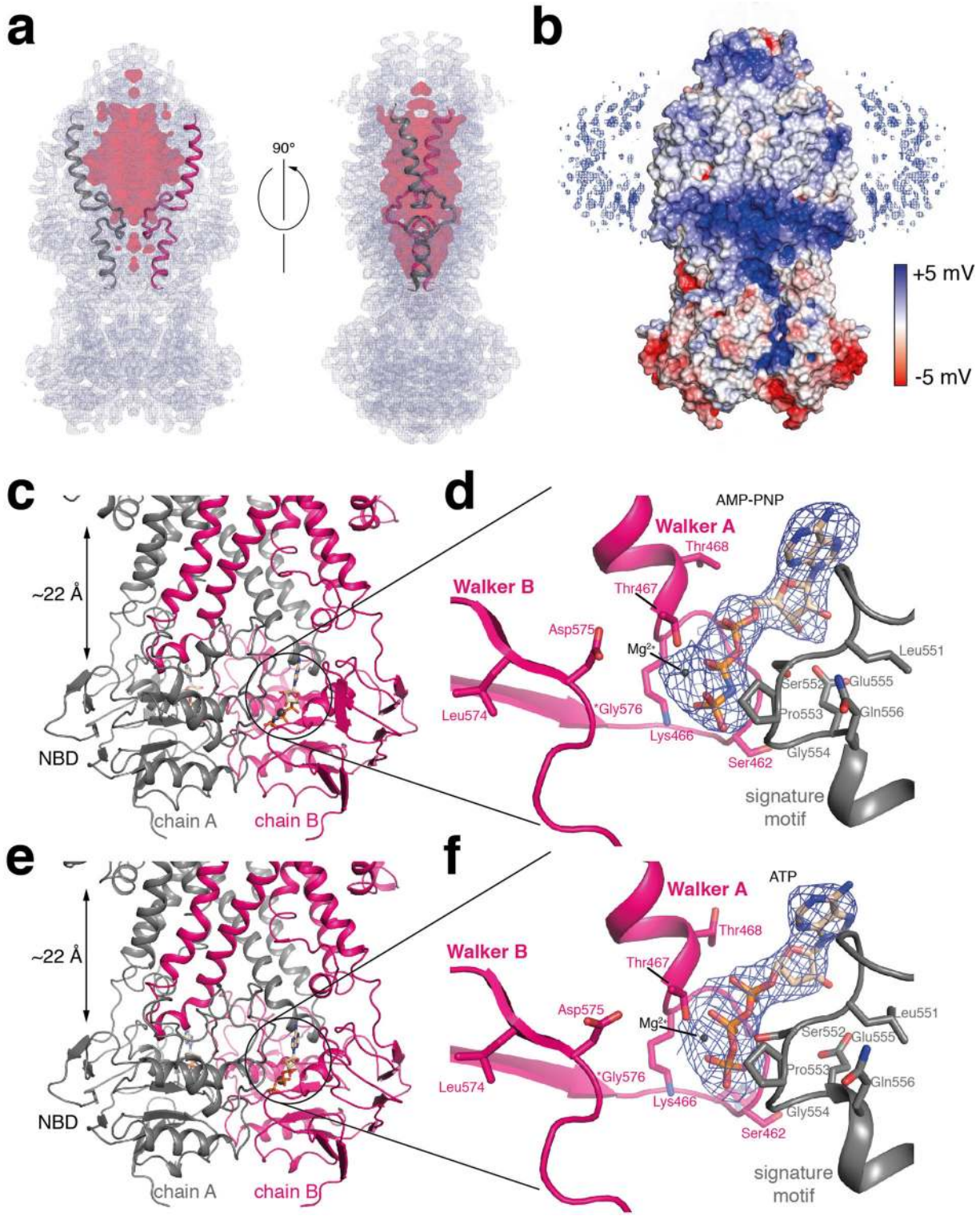

Extended Data Fig. 4 | Seventeen-amino-acid loop insert in TMH3, surface potential of Rv1819c and nucleotide binding domain of Rv1819c(E576G). **a**, Density of Rv1819c(E576G) showing only TMH3 from both protomers (grey and pink) for clarity. The helix is interrupted by a 17-residue loop. For comparison, the density map is layered with the central cross-section of the cavity (red). **b**, Surface representation of Rv1819c(E576G) coloured according to electrostatic potential, showing that the extracellular cap is positively charged. **c**, Closed NBD homodimer (grey, chain A; pink, chain B) with one modelled Mg–AMP-PNP molecule (grey sphere, Mg^{2+}; wheat, carbon atoms; red, oxygen atoms; blue, nitrogen atoms; orange, phosphorus atoms) in each active site. **d**, Protein–nucleotide interaction between the Walker A (chain B) residues Lys466 and Thr469 with AMP-PNP (density shown by blue mesh; $\sigma = 6$) and Thr467 with the Mg^{2+} ion. Residues Ser552 and Glu555 from the signature motif (chain A), which also bind the AMP-PNP molecule, are indicated. The E576G substitution in the Walker B motif is indicated. **e**, **f**, As **c** and **d**, for Rv1819c(E576G), which was purified without the addition of nucleotides. The observed density (blue mesh, $\sigma = 6$) in the pocket is large enough to fit a Mg–ATP molecule.

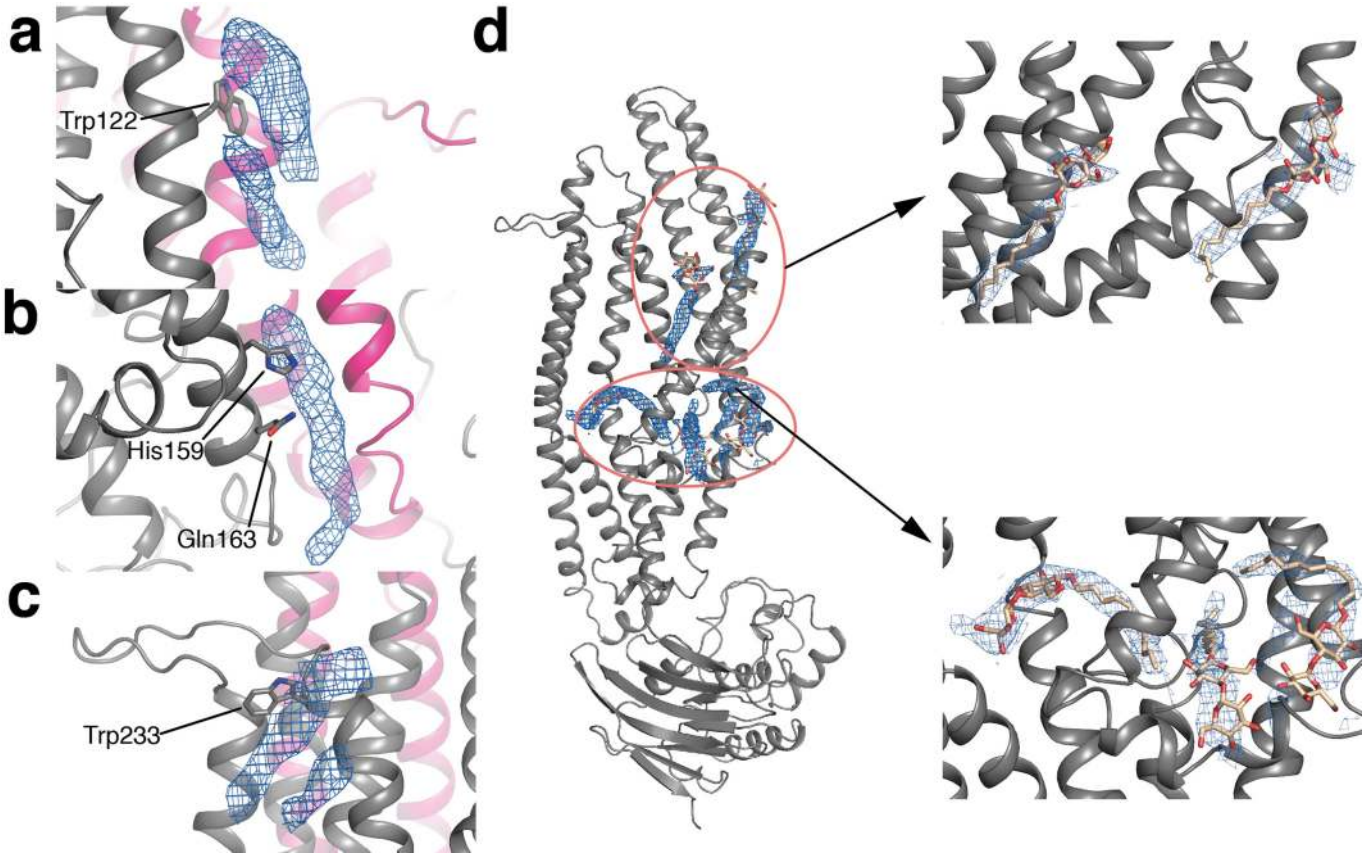

Extended Data Fig. 5 | Modelled DDM molecules and density patches of unclear origin. a–**d**, Densities (blue mesh) rendered at $\sigma = 3.5$ are shown, which are well-defined but cannot be assigned at the current resolution, and others that might originate from DDM molecules (wheat with oxygen atoms red). **a**, Two densities located near Trp122. **b**, Density patch at the interface of the protomers close to His159 and Gln163. **c**, Two densities close to Trp233. **d**, Five putative DDM molecules (only one protomer for clarity).

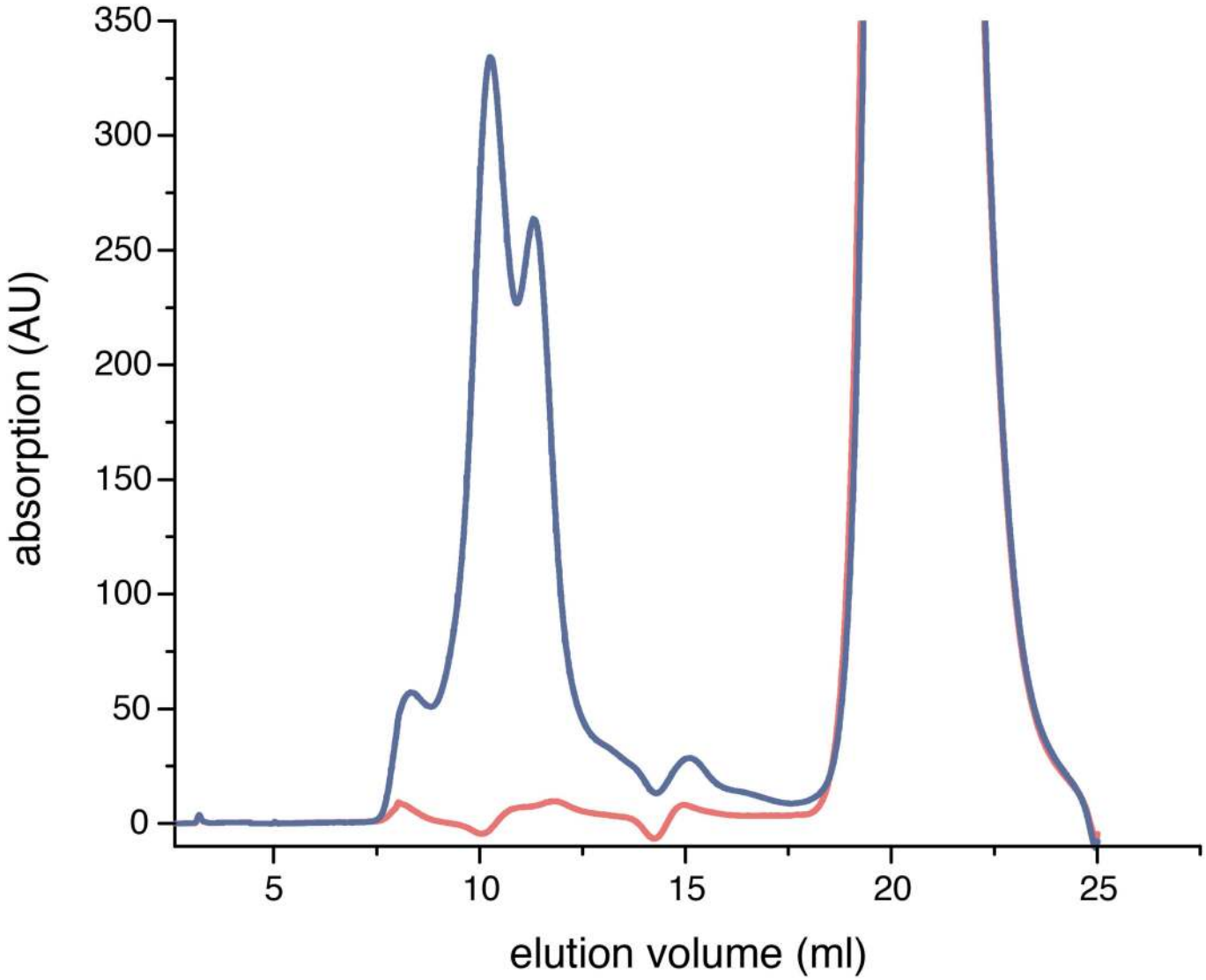

Extended Data Fig. 6 | Elution profile of Rv1819c in the presence of nucleotides and cobalamin. The wild-type protein was purified in the presence of 2 mM cobalamin and 5 mM Mg–ATP during solubilization and affinity chromatography. Elution from the affinity column was performed in the presence of 5 mM Mg–AMP-PNP. The size-exclusion chromatography buffer did not contain substrates. There was no co-elution of cobalamin, which absorbs strongly at 361 nm (red) and eluted between 18 ml and 24 ml, after the protein (280 nm, blue). The wild-type protein eluted as non-native dimers of homodimers (~10 ml elution volume) and the native homodimeric species (~12 ml elution volume).

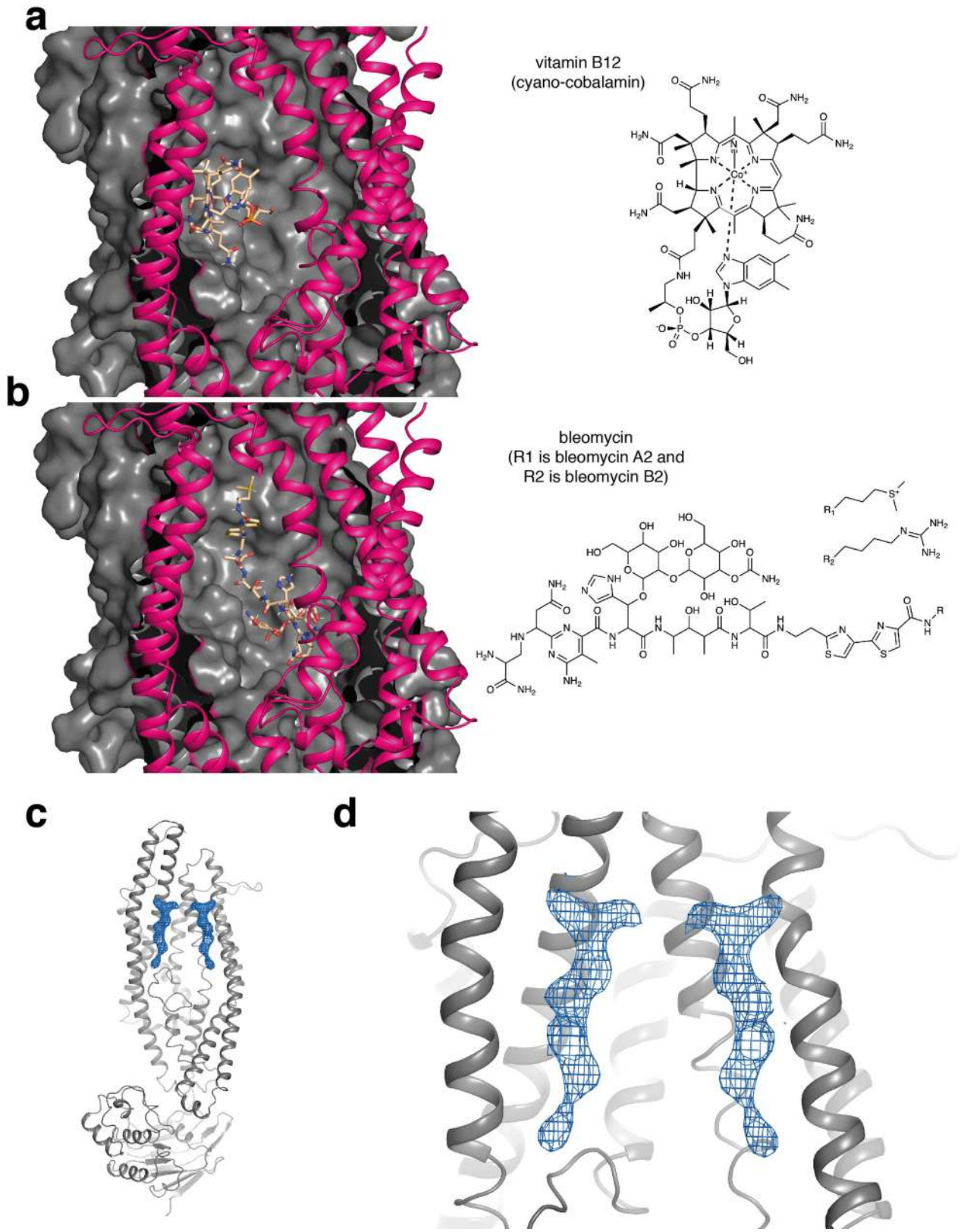

Extended Data Fig. 7 | Cobalamin and bleomycin docked into Rv1819c(E576G) and density patches inside the occluded cavity of Rv1819c(E576G). a, **b**, View through chain B (pink, residues 371–393 were omitted for clarity) into the cavity of Rv1819c. Chain A (grey) is shown as surface and cartoon representation, and cobalamin and bleomycin are shown in stick representation (wheat with oxygen atoms in red, nitrogen atoms in blue, sulfur atoms in yellow and cobalt in light pink). **a**, **b**, Docked cobalamin (**a**, right) and docked bleomycin (**b**, right). **c**, **d**, The two density patches in the cavity, rendered at $\sigma = 5$ and shown as blue mesh. For clarity, only one chain is shown. **c**, View of the entire chain. **d**, Closer view of the densities resembling a potential co-purified peptide.

Extended Data Table 1 | Cryo-EM data collection, refinement and validation statistics

	Rv1819c_E576G Mg-AMP-PNP	Rv1819c_E576G without addition
Data collection and processing		
Voltage (kV)	300	300
Electron exposure (e^-/Å^2)	82	82
Defocus range (μm)	-1.5 to -2.8	-1.5 to -2.8
Pixel size (Å)	0.8521	0.8521
Symmetry imposed	C2	C2
Initial particle images	3,500,000	354,241
Final particle images	314,691	35,890
Map resolution (Å)	3.5	4.3
FSC threshold	0.143	0.143
Refinement		
Initial model used	NBDs 2ONJ (Sav1866)	Rv1819c_E576G
Map-sharpening *B* factor (Å^2)	136	144
Model composition		
Nonhydrogen atoms	10,426	10,076
Protein residues	1,268	1,268
Ligands	14	4
Mean *B* factors (Å^2)		
Protein	72.14	70.67
Ligand	83.81	90.00
R.m.s. deviations		
Bond lengths (Å)	0.009	0.008
Bond angles (°)	1.031	1.090
Validation		
MolProbity score	1.41	1.65
Clash score	2.05	3.67
Poor rotamers (%)	0.57	0.57
Ramachandran plot		
Favored (%)	93.41	91.67
Allowed (%)	6.59	8.33
Disallowed (%)	0.00	0.00

Extended Data Table 2 | Primers used in the study

Primer name	Sequence 5' to 3'
Rv1819c_NcoI_frwd	AAGCCATGGGTCCGAAAC
Rv1819c_cHis8_HindIII_rev	CATCCGCCAAAACAGCCAAGCTTTTA TCAGTGGTGGTGATGGTGATGATGA TGAACTTCTGCCGGTGCTGCTTCAACC
Rv1819c_E576G_frwd	GTTTTTCTGGATGGAAGCACCAGCGC
Rv1819c_E576G_rev	GCGCTGGTGCTTCCATCCAGAAAAAC
sequencing primer I	CTCTACTGTTTCTCCATACCCG
Sequencing primer II	GCTGAAAATCTTCTCTCATCCG

Corresponding author(s): Cornelius Gati
Albert Guskov
Dirk Jan Slotboom

Last updated by author(s): Dec 19, 2019

Reporting Summary

Nature Research wishes to improve the reproducibility of the work that we publish. This form provides structure for consistency and transparency in reporting. For further information on Nature Research policies, see Authors & Referees and the Editorial Policy Checklist.

Statistics

For all statistical analyses, confirm that the following items are present in the figure legend, table legend, main text, or Methods section.

n/a	Confirmed
☐	☒ The exact sample size (*n*) for each experimental group/condition, given as a discrete number and unit of measurement
☐	☒ A statement on whether measurements were taken from distinct samples or whether the same sample was measured repeatedly
☒	☐ The statistical test(s) used AND whether they are one- or two-sided *Only common tests should be described solely by name; describe more complex techniques in the Methods section.*
☒	☐ A description of all covariates tested
☒	☐ A description of any assumptions or corrections, such as tests of normality and adjustment for multiple comparisons
☐	☒ A full description of the statistical parameters including central tendency (e.g. means) or other basic estimates (e.g. regression coefficient) AND variation (e.g. standard deviation) or associated estimates of uncertainty (e.g. confidence intervals)
☒	☐ For null hypothesis testing, the test statistic (e.g. *F*, *t*, *r*) with confidence intervals, effect sizes, degrees of freedom and *P* value noted *Give P values as exact values whenever suitable.*
☒	☐ For Bayesian analysis, information on the choice of priors and Markov chain Monte Carlo settings
☒	☐ For hierarchical and complex designs, identification of the appropriate level for tests and full reporting of outcomes
☒	☐ Estimates of effect sizes (e.g. Cohen's *d*, Pearson's *r*), indicating how they were calculated

Our web collection on statistics for biologists contains articles on many of the points above.

Software and code

Policy information about availability of computer code

Data collection	SerialEM 3.7, SparkControl v2.3, Gen5, ChromLab4, Proteome Discoverer, ChromeLab4
Data analysis	Origin 2015, RELION 3, CtfFind4.1, MotionCor2, Phenix 1.14, Pymol 2.3, Peaks Studio 10, AutoDock4.2, AutoDockTools v1.5, CASTp 3.0 (online server), COOT v0.8.9.2, UCSF Chimera v1.14, MolProbity v4.5, no custom code was used

For manuscripts utilizing custom algorithms or software that are central to the research but not yet described in published literature, software must be made available to editors/reviewers. We strongly encourage code deposition in a community repository (e.g. GitHub). See the Nature Research guidelines for submitting code & software for further information.

Data

Policy information about availability of data

All manuscripts must include a data availability statement. This statement should provide the following information, where applicable:

- Accession codes, unique identifiers, or web links for publicly available datasets
- A list of figures that have associated raw data
- A description of any restrictions on data availability

Atomic coordinates and the cryo-EM map are deposited in the Protein Data Bank and the Electron Microscopy Data Bank under accession numbers 6TQF (AMPPNP), 6TQE (purified without addition), and EMD-10550 (AMP-PNP), EMD-10549 (purified without addition), respectively. Data from this study is available from the corresponding authors upon reasonable request.

Field-specific reporting

Please select the one below that is the best fit for your research. If you are not sure, read the appropriate sections before making your selection.

☒ Life sciences ☐ Behavioural & social sciences ☐ Ecological, evolutionary & environmental sciences

For a reference copy of the document with all sections, see nature.com/documents/nr-reporting-summary-flat.pdf

Life sciences study design

All studies must disclose on these points even when the disclosure is negative.

Sample size	For cobalamin growth assays technical triplicates of biological replicates were used. Bleomycin growth assays were performed as biological triplicates. Malachite green ATPase assay were performed as technical triplicats and coupled ATPase assay was performed as technical triplicates, of which two (in proteoliposomes) additionally as five biological replicates. Because no statistical analysis other than the standard error of the mean between the above mentioned replicates to show the variance between replicates, no sample-size predetermination was required.
Data exclusions	No data was excluded.
Replication	The results were successfully reproduced in multiple and independent experiments.
Randomization	Samples and organisms were not allocated into experimental groups, thus randomization is not relevant for our study. However, single colonies for growth assays were picked randomly.
Blinding	There was no group allocation during data collection and/or analysis making blinding not necessary.

Reporting for specific materials, systems and methods

We require information from authors about some types of materials, experimental systems and methods used in many studies. Here, indicate whether each material, system or method listed is relevant to your study. If you are not sure if a list item applies to your research, read the appropriate section before selecting a response.

Materials & experimental systems

n/a	Involved in the study
☐	☒ Antibodies
☒	☐ Eukaryotic cell lines
☒	☐ Palaeontology
☒	☐ Animals and other organisms
☒	☐ Human research participants
☒	☐ Clinical data

Methods

n/a	Involved in the study
☒	☐ ChIP-seq
☒	☐ Flow cytometry
☒	☐ MRI-based neuroimaging

Antibodies

Antibodies used	Monoclonal Anti-polyHistidine-Peroxidase clone HIS-1 produced in mouse, purified immunoglobulin, Sigma-Aldrich, Cat.Nr. A7058, lot number 073M4815, dilution 1:6000, clone name not applicable
Validation	From manufacturer's website: Anti-polyHistidine (mouse IgG2a isotype) is derived from the HIS-1 hybridoma produced by the fusion of mouse myeloma cells and splenocytes from a mouse immunized with a polyhistidine-tagged fusion protein. The isotype is determined by double diffusion assay using Mouse Monoclonal Antibody Isotyping Reagents (Catalog Number ISO2). Monoclonal anti-polyHistidine, Peroxidase conjugate is prepared by conjugation of horseradish peroxidase to mouse monoclonal anti- polyHistidine purified from ascites fluid of the HIS-1 hybridoma. Monoclonal antibody reacting specifically with poly- histidine may be useful in various immunotechniques, to identify the expression of a polyhistidine fusion protein in bacteria, bacterial lysates, or cells and tissues transfected with a polyhistidinetagged fusion protein expressing vectors.